Article

Mechanisms of 1s Double-Core-Hole Excitation and Decay in Neon

Maksim D. Kiselev [1,2,3,*], Elena V. Gryzlova [1], Sergei M. Burkov [3], Oleg Zatsarinny [4,†] and Alexei N. Grum-Grzhimailo [1]

1 Skobeltsyn Institute of Nuclear Physics, Lomonosov Moscow State University, 119991 Moscow, Russia; gryzlovaev@depni.sinp.msu.ru (E.V.G.); grum@sinp.msu.ru (A.N.G.-G.)
2 Faculty of Physics, Lomonosov Moscow State University, 119991 Moscow, Russia
3 Laboratory for Modeling of Quantum Processes, Pacific National University, 680035 Khabarovsk, Russia; 004130@pnu.edu.ru
4 Department of Physics and Astronomy, Drake University, Des Moines, IA 50311, USA; oleg.zatsarinny@drake.edu
* Correspondence: md.kiselev@physics.msu.ru
† Deceased.

Abstract: The formation and decay of double-core-hole (DCH) states of the neon ion irradiated by an intense electromagnetic x-ray field are studied theoretically. In the present research DCH formation is the result of sequential absorption of two photons with the creation of an intermediate ion. Detailed calculations of the partial decays and probabilities of shake-ups at the atomic and ionic ionization stages are presented. The angular distribution of photoelectrons corresponding to various residual ionic states are calculated. Specifically, we predict the lack of any photoelectrons corresponding to the residual ionic state $1s^1 2s^2 2p^n mp^{n'\, 2S_f+1}D$ in the direction of the electric field polarization. Dynamical competition between single-core-hole state decay and excitation is analyzed and pulse parameters corresponding to various dynamical regimes are found.

Keywords: photoionization; double-core-hole; R-matrix; multiple ionization; ions; free-electron laser; neon; photoelectron spectroscopy; rate equations

1. Introduction

Investigations of formation and decay double-core-hole states (DCH) are of great importance for both fundamental physics and applications such as radioactive damage of biological samples for coherent diffraction imaging [1–3]. They are crucial for molecular spectroscopy because of the large chemical shifts in DCH states. These states may eventually be generated in nuclear reactions [4], and for some time they have been studied in the single-photon ionization by synchrotron radiation with shake-up process to discrete states [5–7] (also addressed as hypersatellites), or shake-up to continuum (direct multiple ionization) [8,9]. Indirect methods of studying DCH states, such as photoabsorption [10,11], x-ray emission [12], and a coincidence scheme [13], have also been developed.

With the advent of Free-Electron Lasers (FELs), these states became available in the nonlinear *sequential* ionization regime when there is a time delay δt between the formation of single and double core-hole states, and there is a dynamical competition (depending on pulse intensity and duration) between the Auger decay of single-core-hole states (SCH) and excitation to double-core-hole states [14–16]. Competition of direct and sequential two-photon multiple ionization mechanism was a subject of numerous investigations [17–19]. In the present research we expect that sequential mechanism is dominant due to resonant enhancement, that confirms by experimental observation in [16].

From a theoretical point of view, the description of states with K-vacancy(ies) is very challenging. The ionic states involved contain at least two open shells. Accurate calculations of the states should account for the re-arrangement of the electronic shells after

inner-shell ionization or excitation, and for electron correlations especially in valence shells. There are many calculations for the SCH $1s^{-1}np$ configuration [20–24] and a thorough review and updated calculations for the Ne atom, together with an interpretation of the findings presented in [25]. On the other hand, much less researches have been reported for the DCH $1s^{-2}np$ configuration [7,26,27].

In the present manuscript, an extended theoretical discussion of the DCH states is presented. Since investigations of such exotic systems are already planned, our results should be interesting for future experiments at XFELs.

The possible pathways of multiple ionization of neon by a strong intense x-ray pulse are presented in Figure 1. All the processes are initiated by ionization of the inner atomic shell $1s$, and the emitted electron has the energy $\omega - IP_1$. (a) If the photon energy is below the Ne^+ $1s$-shell ionization threshold, either Auger decay to a Ne^{2+} state occurs or resonant excitation of $1s$ to an np state. The latter process becomes dominant with increasing pulse intensity. The excited states may decay to a variety of Ne^{2+} states via processes including: Auger, two-to-one shake-up, conjugate shake-up, etc. (b) If the photon energy is above the Ne^+ $1s$-shell ionization threshold, the Auger decay of $1s^12s^22p^6\,^2S$ competes with ionization to Ne^{2+} with subsequent decay to Ne^{3+}.
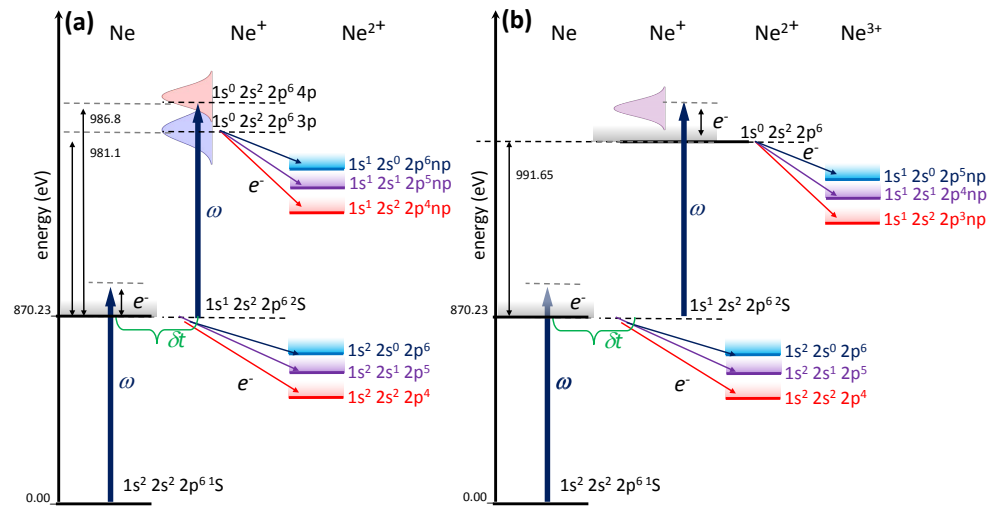
Figure 1. Multiple ionization of Ne for photon energies below (**a**) or above (**b**) the Ne^+ $1s$-shell ionization threshold of $991.65\,\text{eV}$. The ionization potential of the atomic $1s$-shell, $IP_1 = 870.23\,\text{eV}$, was taken from [28].

2. Models and the Photoabsorption Spectrum

We performed photoionization calculations in the framework of the nonrelativistic *LS*-coupling approximation by means of the B-spline R-matrix (BSR) approach [29]. Each individual electron wave-function in the initial and final states was obtained in the multi-configuration Hartree-Fock approximation [30]. The photoabsorption cross section of Ne^+ $1s^12s^22p^6$ for photon energies covering the region of autoionizing series $1s^{-2}np$ ($n = 3, 4, \ldots, \infty$) in two models ($\mathcal{P}$ and $\mathcal{SP}$, see below for details) is shown in Figure 2. In both models, the initial state of Ne^+ $1s^12s^22p^6$ is a pure ^2S state, while the sets of final doubly-charged Ne^{2+} states differ in the following ways:

(i)   in the first model we include only $\mathcal{P}$articipator configurations ($\mathcal{P}$-model): $1s^12s^22p^5, 1s^02s^22p^6$ with all possible total orbital and spin angular momenta;

(ii) in the second model we add to the $\mathcal{P}$-model $\mathcal{S}$pectator configurations ($\mathcal{SP}$-model) with an np-electron (n = 3–8) and also configurations with $3s$ and $3d$ electrons, which results in the following set:

$$1s^12s^22p^5, 1s^12s^12p^6, 1s^02s^22p^6,$$

$$\left[1s^12s^22p^4, 1s^12s^02p^6, 1s^02s^22p^5, 1s^12s^12p^5, 1s^02s^12p^6\right]3s/3d,$$

$$\left[1s^12s^22p^4, 1s^12s^02p^6, 1s^02s^22p^5, 1s^12s^12p^5, 1s^02s^12p^6\right]np\,(n=3-8).$$
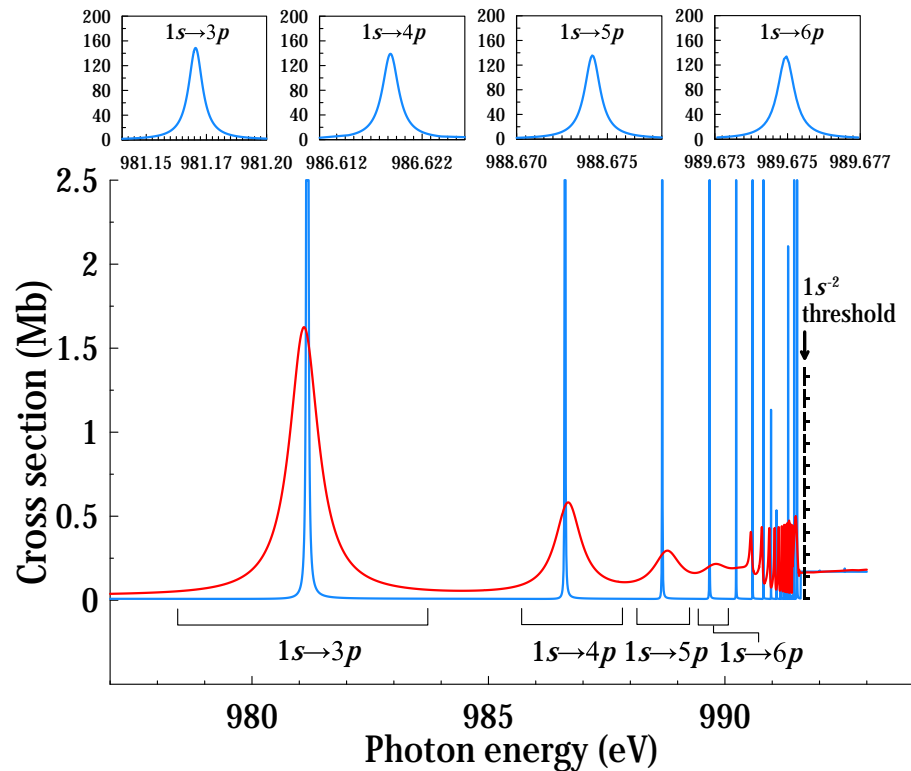
Figure 2. Photoabsorption spectrum in the simple ($\mathcal{P}$) and extended ($\mathcal{SP}$) models, shown by the blue and red lines, respectively. The insets show the detailed spectrum in the $\mathcal{P}$-model.

It is clearly seen from Figure 2 that the inclusion of spectator decay states is crucial for the shape of the resonance structures. When only participator decay states are included in the calculation ($\mathcal{P}$-model), we see a series of narrow and spiky peaks converging to the $1s$-shell double ionization threshold of neon. In contrast, when we additionally include spectator configurations ($\mathcal{SP}$-model), each resonance from the series becomes much wider. The narrowness of each peak can be described by its width Γ and, according to the *Uncertainty Principle*, one can estimate the lifetime τ of a particular resonance as $\tau \sim \hbar/\Gamma$. Consequently, there is a strong indication that neglecting the np-spectator decay channels leads to a crucial overestimate of the DCH $1s^{-2}np$-resonance lifetime. A comparison between the $1s^{-2}np$-resonance widths and corresponding lifetimes obtained in the two models is presented in Table 1.

Looking at Table 2, one can see that in the more accurate $\mathcal{SP}$-model less than 3% of the decays are caused by participator or shake-down processes; 69.7% are spectator decays affecting the valence $2p$-shell only, with dominant final states corresponding to larger statistical weights (line 10—^3D and line 12—^3F); spectator decays affecting the $2s$-shell with creation of both single and double $2s$-hole states contribute about 16.5%; and finally 11.67% go with shake-up processes $3p \rightarrow np\,(n \geq 4)$.

Table 3 in general confirms the above statements, with the only exception that for the $1s^{-2}4p$ state shake-down with $4p \rightarrow 3p$ consists of essential 8.7%. The tendencies are

not surprising, because the overlaps between the $4p$ and $3p$ orbitals are larger than for $3p$ and $2p$.

Table 1. Widths and lifetimes for the $1s^{-2}np$ ($n = 3$–6) states obtained in the two models.

Configuration	Model $\mathcal{P}$	Model $\mathcal{SP}$	Model $\mathcal{P}$	Model $\mathcal{SP}$
	Width, meV		Lifetime, fs	
$1s^{-2}3p$	5.6	740	117.5	0.88
$1s^{-2}4p$	2.3	650	286.1	1.02
$1s^{-2}5p$	1.1	-	598.4	-
$1s^{-2}6p$	0.57	-	1154.8	-

Table 2. $1s^{-2}3p$ autoionizing branching ratios (BR, in %) for the Ne$^+$ states obtained in the two models.

Target	Configuration	Term	BR (Model $\mathcal{P}$)	BR (Model $\mathcal{SP}$)
		$1s^0 2s^2 2p^6 3p$		
1	$1s^1 2s^2 2p^5$	^3P	62.0	1.12
2	$1s^1 2s^2 2p^5$	^1P	38.0	0.60
3	$1s^1 2s^1 2p^6$	^3S	-	0.68
4	$1s^1 2s^1 2p^6$	^1S	-	0.29
5	$1s^1 2s^2 2p^4 [^2S] 3p$	^1P	-	1.85
6	$1s^1 2s^2 2p^4 [^2S] 3p$	^3P	-	6.77
7	$1s^1 2s^2 2p^4 [^2P] 3p$	^1P	-	1.40
8	$1s^1 2s^2 2p^4 [^2P] 3p$	^3P	-	2.81
9	$1s^1 2s^2 2p^4 [^2D] 3p$	^1D	-	4.93
10	$1s^1 2s^2 2p^4 [^2D] 3p$	^3D	-	15.22
11	$1s^1 2s^2 2p^4 [^2D] 3p$	^1F	-	7.23
12	$1s^1 2s^2 2p^4 [^2D] 3p$	^3F	-	21.61
13	$1s^1 2s^2 2p^4 [^4P] 3p$	^3D	-	0.003
14	$1s^1 2s^2 2p^4 [^4P] 3p$	^3P	-	0.62
15	$1s^1 2s^2 2p^4 [^2D] 3p$	^3P	-	4.70
16	$1s^1 2s^2 2p^4 [^2D] 3p$	^1P	-	2.15
17	$1s^1 2s^2 2p^4 [^2P] 3p$	^3D	-	0.19
18	$1s^1 2s^2 2p^4 [^2P] 3p$	^1D	-	0.18
19	$1s^1 2s^1 [^1S] 2p^5 [^2P] 3p$	^3S	-	0.62
20	$1s^1 2s^1 [^1S] 2p^5 [^2P] 3p$	^3D	-	3.60
21	$1s^1 2s^1 [^1S] 2p^5 [^2P] 3p$	^1D	-	1.23
22	$1s^1 2s^1 [^1S] 2p^5 [^2P] 3p$	^1P	-	0.74
23	$1s^1 2s^1 [^1S] 2p^5 [^2P] 3p$	^1S	-	0.32
24	$1s^1 2s^1 [^1S] 2p^5 [^2P] 3p$	^3P	-	2.21
25	$1s^1 2s^1 [^3S] 2p^5 [^2P] 3p$	^3D	-	2.06
26	$1s^1 2s^1 [^3S] 2p^5 [^2P] 3p$	^3P	-	1.06
27	$1s^1 2s^1 [^3S] 2p^5 [^2P] 3p$	^1P	-	0.44
28	$1s^1 2s^1 [^3S] 2p^5 [^4P] 3p$	^3D	-	5×10^{-4}
29	$1s^1 2s^1 [^3S] 2p^5 [^4P] 3p$	^3P	-	3×10^{-4}
30	$1s^1 2s^1 [^3S] 2p^5 [^4P] 3p$	^3S	-	0.02
31	$1s^1 2s^1 [^3S] 2p^5 [^2P] 3p$	^1S	-	0.14
32	$1s^1 2s^1 [^3S] 2p^5 [^2P] 3p$	^1D	-	0.70
33	$1s^1 2s^0 2p^6 3p$	^3P	-	2.45
34	$1s^1 2s^0 2p^6 3p$	^1P	-	0.84
	Sum		**100.0**	**88.33**

Table 3. $1s^{-2}4p$ autoionizing branching ratios (BR, in %) for the Ne^+ states obtained in the two models.

Target	Configuration	Term	BR (Model $\mathcal{P}$)	BR (Model $\mathcal{SP}$)
		$1s^02s^22p^64p$		
1	$1s^12s^22p^5$	^3P	96.5	1.70
2	$1s^12s^22p^5$	^1P	3.5	0.55
3	$1s^12s^12p^6$	^3S	-	2.05
4	$1s^12s^12p^6$	^1S	-	0.38
5	$1s^12s^22p^4[^2S]4p$	^1P	-	1.59
6	$1s^12s^22p^4[^2S]4p$	^3P	-	4.64
7	$1s^12s^22p^4[^2P]4p$	^1P	-	0.04
8	$1s^12s^22p^4[^2P]4p$	^3P	-	0.65
9	$1s^12s^22p^4[^2D]4p$	^1D	-	3.46
10	$1s^12s^22p^4[^2D]4p$	^3D	-	10.00
11	$1s^12s^22p^4[^2D]4p$	^1F	-	4.64
12	$1s^12s^22p^4[^2D]4p$	^3F	-	13.42
13	$1s^12s^22p^4[^4P]4p$	^3D	-	2×10^{-4}
14	$1s^12s^22p^4[^4P]4p$	^3P	-	0.04
15	$1s^12s^22p^4[^2D]4p$	^3P	-	2.94
16	$1s^12s^22p^4[^2D]4p$	^1P	-	1.65
17	$1s^12s^22p^4[^2P]4p$	^3D	-	0.003
18	$1s^12s^22p^4[^2P]4p$	^1D	-	0.014
19	$1s^12s^1[^1S]2p^5[^2P]4p$	^3S	-	0.72
20	$1s^12s^1[^1S]2p^5[^2P]4p$	^3D	-	3.77
21	$1s^12s^1[^1S]2p^5[^2P]4p$	^1D	-	1.30
22	$1s^12s^1[^1S]2p^5[^2P]4p$	^1P	-	0.79
23	$1s^12s^1[^1S]2p^5[^2P]4p$	^1S	-	0.34
24	$1s^12s^1[^1S]2p^5[^2P]4p$	^3P	-	2.32
25	$1s^12s^1[^3S]2p^5[^2P]4p$	^3D	-	2.21
26	$1s^12s^1[^3S]2p^5[^2P]4p$	^3P	-	1.36
27	$1s^12s^1[^3S]2p^5[^2P]4p$	^1P	-	0.48
28	$1s^12s^1[^3S]2p^5[^4P]4p$	^3D	-	3.1×10^{-4}
29	$1s^12s^1[^3S]2p^5[^4P]4p$	^3P	-	1.4×10^{-4}
30	$1s^12s^1[^3S]2p^5[^4P]4p$	^3S	-	0.01
31	$1s^12s^1[^3S]2p^5[^2P]4p$	^1S	-	0.14
32	$1s^12s^1[^3S]2p^5[^2P]4p$	^1D	-	0.77
33	$1s^12s^02p^64p$	^3P	-	2.62
34	$1s^12s^02p^64p$	^1P	-	0.91
	Sum		**100.0**	**65.51**

Strictly speaking, there are other mechanisms due to which the same final states (see the scheme in Figure 1 and discussions below) could be produced in neon and its ions. These mechanisms are connected to ionization of the neutral atom, or of the ion SCH state $1s^{-1}$, accompanied by a shake-up process to the np-state. In order to evaluate how important such mechanisms are, we calculated the probabilities for shake-up processes in atomic (see Table 4) and ionic (see Table 5) ionization. Our approach for such calculations is based on the $\mathcal{SP}$-model, i.e., the initial atomic (or ionic SCH) state is a pure state while the final single ionic (or double ionic) states are mixed with each other. The difference compared to $\mathcal{SP}$-model described above is in the omission of states with $3s/3d$-electrons and in only considering np-electron states with $n \leq 5$. [We label this approach as the $\mathcal{SP}^{(0)}$-model.] From Tables 4 and 5 it is clearly seen that (i) the probability of the considered mechanisms is strongly suppressed in the calculation within the $\mathcal{SP}^{(0)}$-model and the dominating mechanism is direct ionization of the inner shell; and (ii) the more efficient shake-up goes to the ^2S (for the atom) and ^1S (for the ion) term of the residual ion. The latter means that the core remains unaffected by electron correlation.

Table 4. Probabilities (in %) for shake-up processes in atomic ionization for the extensive model at photon energy $\hbar\omega = 1080$ eV.

Target	Configuration	Term	Probability (Model $\mathcal{SP}^{(0)}$)
1	$1s^1 2s^2 2p^6$	^2S	**93.60**
2	$1s^1 2s^2 2p^5 [^3P] 3p$	^2D	0.07
3	$1s^1 2s^2 2p^5 [^3P] 3p$	^2P	0.03
4	$1s^1 2s^2 2p^5 [^3P] 3p$	^2S	0.90
5	$1s^1 2s^2 2p^5 [^1P] 3p$	^2D	0.08
6	$1s^1 2s^2 2p^5 [^1P] 3p$	^2P	0.017
7	$1s^1 2s^2 2p^5 [^1P] 3p$	^2S	1.40
	Sum (3p)		**2.50**
8	$1s^1 2s^2 2p^5 [^3P] 4p$	^2D	0.02
9	$1s^1 2s^2 2p^5 [^3P] 4p$	^2P	0.012
10	$1s^1 2s^2 2p^5 [^3P] 4p$	^2S	1.22
11	$1s^1 2s^2 2p^5 [^1P] 4p$	^2D	0.021
12	$1s^1 2s^2 2p^5 [^1P] 4p$	^2P	0.006
13	$1s^1 2s^2 2p^5 [^1P] 4p$	^2S	1.16
	Sum (4p)		**2.44**
14	$1s^1 2s^2 2p^5 [^3P] 5p$	^2D	0.01
15	$1s^1 2s^2 2p^5 [^3P] 5p$	^2P	0.005
16	$1s^1 2s^2 2p^5 [^3P] 5p$	^2S	0.97
17	$1s^1 2s^2 2p^5 [^1P] 5p$	^2D	0.009
18	$1s^1 2s^2 2p^5 [^1P] 5p$	^2P	0.003
19	$1s^1 2s^2 2p^5 [^1P] 5p$	^2S	0.45
	Sum (5p)		**1.45**

Table 5. Same as Table 4 for ionization of the $1s^1 2s^2 2p^6 \, ^2S$ Ne$^+$ ion.

Target	Configuration	Term	Probability (Model $\mathcal{SP}^{(0)}$)
1	$1s^0 2s^2 2p^6$	^1S	**92.20**
2	$1s^0 2s^2 2p^5 3p$	^3D	0.87
3	$1s^0 2s^2 2p^5 3p$	^3P	0.35
4	$1s^0 2s^2 2p^5 3p$	^3S	0.25
5	$1s^0 2s^2 2p^5 3p$	^1D	0.13
6	$1s^0 2s^2 2p^5 3p$	^1P	0.04
7	$1s^0 2s^2 2p^5 3p$	^1S	2.60
	Sum (3p)		**4.24**
8	$1s^0 2s^2 2p^5 4p$	^3D	0.33
9	$1s^0 2s^2 2p^5 4p$	^3P	0.15
10	$1s^0 2s^2 2p^5 4p$	^3S	0.08
11	$1s^0 2s^2 2p^5 4p$	^1D	0.08
12	$1s^0 2s^2 2p^5 4p$	^1P	0.025
13	$1s^0 2s^2 2p^5 4p$	^1S	0.98
	Sum (4p)		**1.65**
15	$1s^0 2s^2 2p^5 5p$	^3D	0.17
18	$1s^0 2s^2 2p^5 5p$	^3P	0.08
14	$1s^0 2s^2 2p^5 5p$	^3S	0.03
16	$1s^0 2s^2 2p^5 5p$	^1D	0.05
17	$1s^0 2s^2 2p^5 5p$	^1P	0.03
19	$1s^0 2s^2 2p^5 5p$	^1S	1.58
	Sum (5p)		**1.94**

3. Photoelectron Spectrum and Angular Distribution

We now simulate photoelectron spectra (PES) under the assumption of an "ideal" setup, where the photon bandwidth and electron detector resolution are about 100 meV each to perfectly resolve all the DCH resonances. In order to simplify the analysis, we represent all the PES for the photon energy ranging from 975 eV to 995 eV (in steps of 0.1 eV) by the false color 2D-map in the photoelectron energy region 865 eV to 890 eV in Figure 3. In that figure, one can clearly identify groups of lines corresponding to particular $1s^{-2}np$-resonances. The diagonal features on the 2D-map correspond to particular prevailing final states. When the photon energy is tuned to the $n = 3$ resonance (981.1 eV), the $1s^{-2}3p \rightarrow 1s^{-1}2p^{-2}3p$ (spectator) and the $1s^{-2}3p \rightarrow 1s^{-1}2p^{-2}4p$ (shake-up) channels are dominant. At the same time there is a weak (but nonzero) contribution at the electron energy of ~ 886 eV from the $1s^{-2}3p \rightarrow 1s^{-1}2p^{-1}$ process, in which the $3p$ electron is a participator. Tuning the photon energy to the higher $n = 4$ resonance (986.8 eV), we see the same tendency, i.e., the $1s^{-2}4p \rightarrow 1s^{-1}2p^{-2}4p$ (spectator) and $1s^{-2}4p \rightarrow 1s^{-1}2p^{-2}5p$ (shake-up) channels dominate with prevailing spectator decay, and there are also small lines from the $1s^{-2}4p \rightarrow 1s^{-1}2p^{-2}3p$ (shake-down) decay channel in the vicinity of electron energy $\sim$886–887 eV. Going further to $n \geq 5$ the trend described above persists with only slightly increasing influence of the shake-down processes.
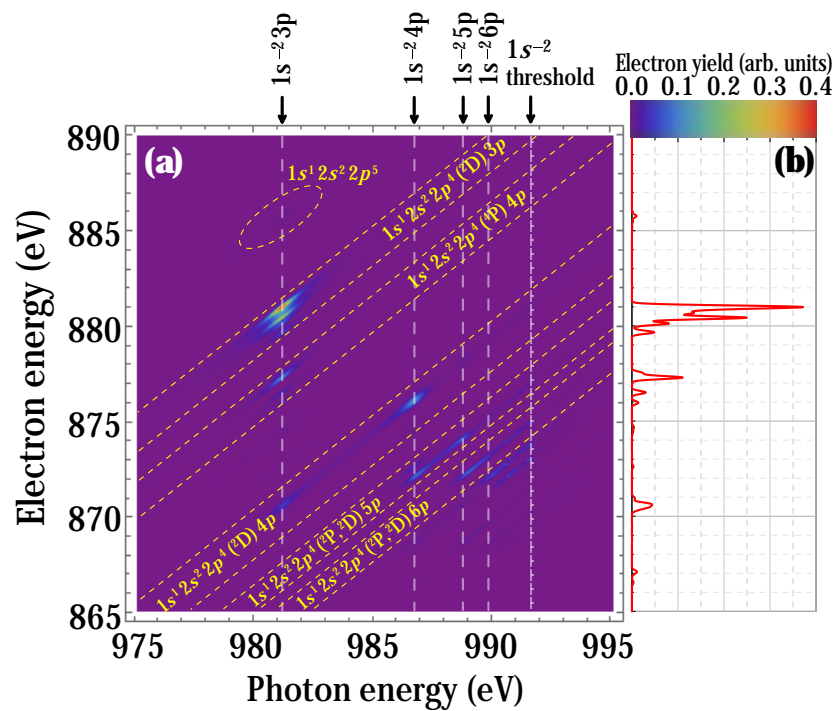

Figure 3. (**a**) Simulated resonance map for a narrow pulse-width (0.1 eV) and high-resolution detector (0.1 eV). (**b**) Calculated photoelectron spectrum (red line) at a photon energy of 981.1 eV corresponding to the calculated $1s^{-2}3p$ resonance excitation energy. This line corresponds to a section in (**a**) at the given excitation photon energy.

Figure 4 exhibits simulated spectra for three angles of observation: parallel $\theta = 0°$, magic $\theta = \arccos[1/\sqrt{3}] = 54.7°$ and orthogonal $\theta = 90°$ to the polarization vector of the field. Because the $1s^{1}2s^{2}2p^{6}\,[^{2}S]$ state of Ne^{+} cannot be polarized, the photoelectron angular distribution (PAD) is solely defined by the second Legendre polynomial $P_2(\cos\theta)$, i.e.,

$$W(\theta) = W_0(1 + \beta P_2(\cos\theta)). \tag{1}$$

When the signal at $0°$ is higher than for the magic angle, the angular anisotropy parameter is positive. This situation is realized for the lines G and H, corresponding to $^{1,3}F$ terms of the residual ion, while for the lines E and F, corresponding to $^{1,3}D$ terms,

the situation is opposite. The lines A, B, C, D corresponding to $^{1,3}P$ terms are practically isotropic. Because we consider ionization of the $1s^1 2s^2 2p^6\,^2S$ state, the final system of "ion+electron" has an angular momentum of 1 (i.e., it forms a P state) and the s-wave is only allowed for residual ions with the $^{2S_f+1}P$ term. Therefore, the PAD for the lines E, F, G, H is determined by the d-wave, besides the g-wave provides a surprisingly large contribution for G and H. Neglecting the latter, the anisotropy parameter β assumes the analytical values of $\beta = -1$ for E and F and $\beta = 1/7$ for G and H, respectively. The presence of the s-wave in the PAD for lines A, B, C, D naturally makes them more isotropic. Note that $\beta = -1$ for the $^{2S_f+1}D$ term of the residual ion results in the complete elimination of the corresponding lines in the spectrum observed parallel to field polarization (see the red line in Figure 4).
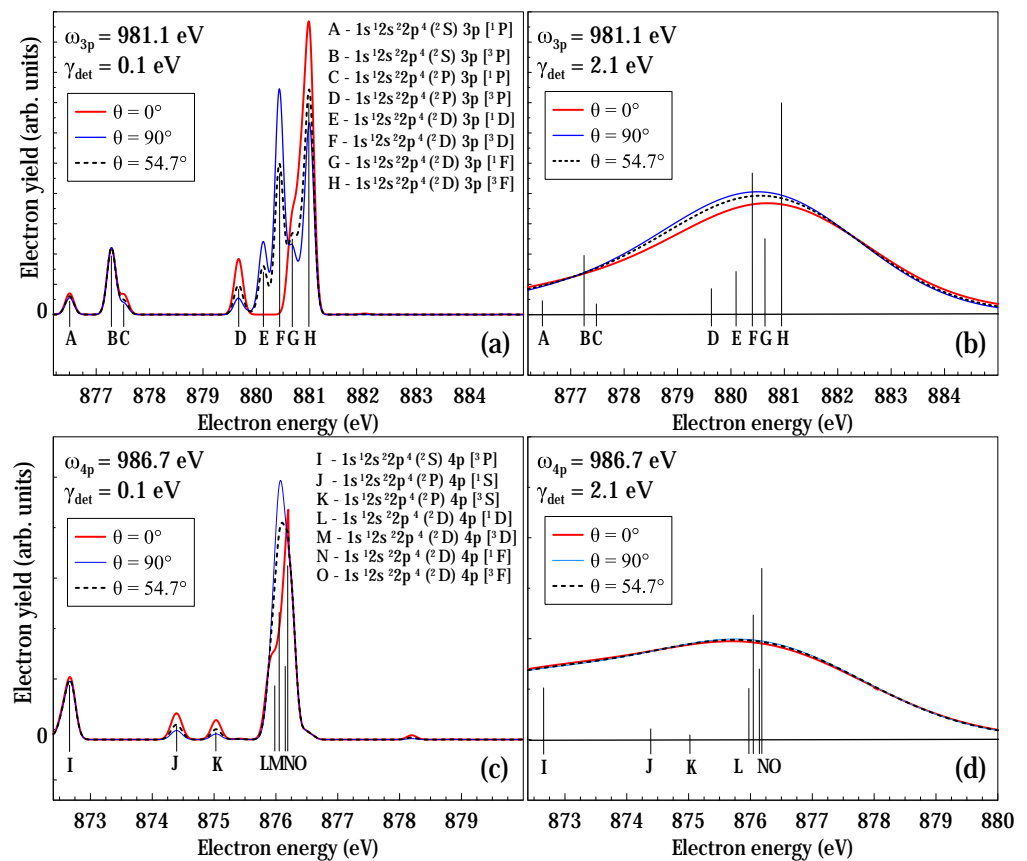
Figure 4. Photoelectron spectrum for various angles: along laser polarization vector ($\theta = 0°$), magic angle ($\theta = \arccos[1/\sqrt{3}] = 54.7°$) and orthogonal to the polarization ($\theta = 90°$). Left column (**a**,**c**)—results for high-resolution detector (0.1 eV); Right column (**b**,**d**)—currently realistic detector (2.1 eV, [16]). For the PES on (**a**,**b**) the incident photon energy is tuned to the $1s^{-2}3p$-resonance; for the PES on (**c**,**d**)—to the $1s^{-2}4p$-resonance.

However, convolving the spectrum with a currently more realistic experimental resolution (like resolution in the experiment [16]) diminishes the angular anisotropy, because the strongest lines have different angular dependencies. For ionization with $4p$ (and higher) spectators, an angular dependence does not appear even for the "ideal" detector.

4. Population of Atomic and Ionic States in Multiple Ionization

The calculations of the widths and branching ratios presented here allow us to analyze the time-dependent population of different Ne and Ne$^+$ states and, therefore, the relative intensity of the photoelectron lines corresponding to different processes. The way how the system evolves depends on the photon flux density (i.e., the number of photons per

surface per time) and the pulse duration. We assumed a temporal Gaussian distribution of the incident flux, i.e.,

$$j(t) = j_0 \exp(-4 \ln 2 \, t^2 / \tau^2), \tag{2}$$

where τ is the full width at half maximum of the pulse. The photon flux is related to the fluence F, i.e., to the integral number of photons per 1 Å^2 in the entire pulse, according to

$$j_0 = \frac{2\sqrt{\ln 2} \, F}{\sqrt{\pi} \, \tau} = 0.0063634 \frac{F \, [\text{ph}/\text{Å}^2]}{\tau \, [fs]}. \tag{3}$$

To analyse the system evolution we applied the method of solving the rate equations as described in [31]. Figure 5 displays the populations of the different states calculated at a high photon fluence $F = 1000 \, \text{ph}/\text{Å}^2$ and varying pulse durations of $\tau =$15 fs, 30 fs and 60 fs, respectively; the photon energy is in resonance with the $1s \to 3p$ transition in Ne$^+$. Because the overall number of photons is the same, increasing the pulse duration means decreasing the flux. For this reason, the population of the ground state tends towards the same value (black lines in panels (a,b,c) of Figure 5). For the singly-charged ion with inner-shell vacancy $1s^1 2s^2 2p^6$ (red lines), there is competition between Auger decay to different Ne^{2+} states (red dashed lines) and excitation to Ne$^+ 1s^0 2s^2 2p^6 3p$ (blue lines). Because of the short lifetimes of both Ne$^+$ resonances ($1s^{-1}$ and $1s^{-2} 3p$), no population in these states should remain at the end of the pulse. Figure 5a shows the case with a duration such that the probabilities for the intermediate ion to decay or to be excited are equal; for longer pulses (Figure 5b) the intermediate ion has enough time to decay and the products of the decay of SCH $1s^1 2s^2 2p^6$ are significant; for shorter pulse (Figure 5c) the excitation mechanism is more effective and the products of the decay of DCH $1s^0 2s^2 2p^6 3p$ resonance dominate.
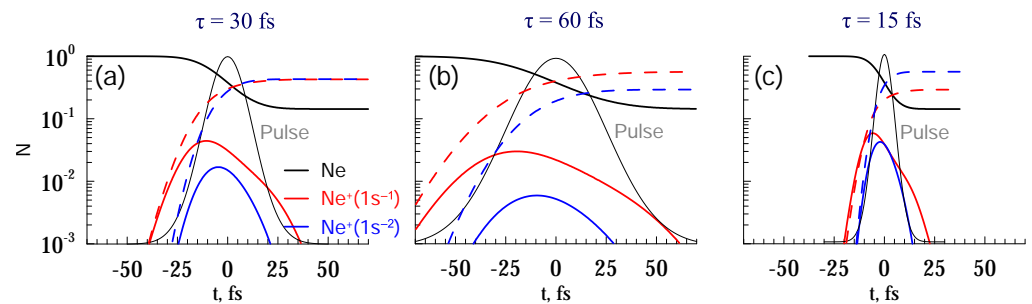
Figure 5. Population of different species in neon multiple ionization by a pulse with ω corresponding to $1s \to 3p$ Ne$^+$ excitation: the black line marks the ground state; red—Ne$^+ (1s^1 2s^2 2p^6)$; blue—Ne$^+ (1s^0 2s^2 2p^6 3p)$; the dashed lines represent the summed population of Ne^{2+} states originating from SCH Ne$^+ (1s^1 2s^2 2p^6)$ (red) and DCH Ne$^+ (1s^0 2s^2 2p^6 3p)$ (blue) resonances. The fluence $F = 1000 \, \text{ph}/\text{Å}^2$ and the panels are for different pulse durations: (**a**) $\tau = 30$ fs; (**b**) $\tau = 60$ fs, (**c**) $\tau = 15$ fs.

In order to summarize and clarify the general tendencies, we sketch in Figure 6 a variety of competitive channels that are possible in neon irradiated by an intense XUV field. This summary is based on Tables 1–5. The threshold and excitation energies, and the relative probabilities (when possible) are marked.
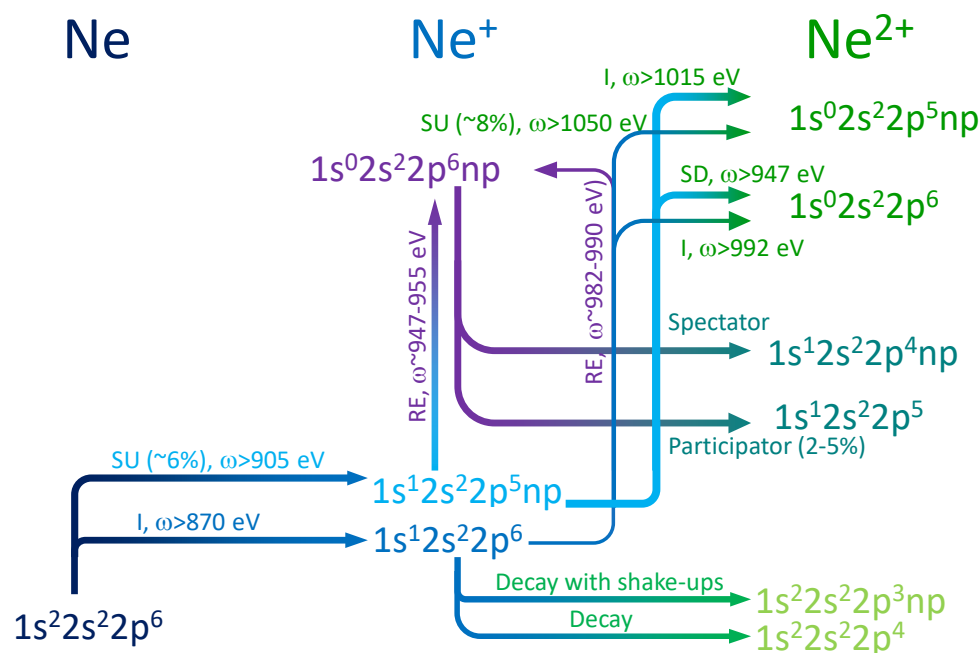
Figure 6. Scheme of possible processes in neon irradiated by an intense XUV field: 'I' marks ionization, 'SU' ionization with shake-ups, 'SD' ionization with shake-down, 'RE' resonance excitation. Furthermore, 'spectator' and 'participator' indicate the type of Auger decay.

5. Conclusions

Extensive calculations of energy levels, widths, and branching ratios of double-core-hole states of Ne^+ were presented. The role of spectator and participator channels were analyzed, and it was shown that the most important among those are spectator-type channels affecting only the valence $2p$-shell. Second in importance are spectator-type channels affecting the valence $2s$-shell (single and double $2s$-holes together). Processes involving np-electrons as participators (including shake-ups and shake-downs) contribute less than 15% altogether.

We also investigated the role of shake-up satellites in direct atomic and ionic ionization from the inner $1s$-shell. These were found to be not essential in forming double-core-hole states.

Finally, we calculated photoelectron angular distributions after inner-shell ionization of Ne^+ and found that the angular anisotropy parameter for the $1s^1 2s^2 2p^n mp^{n'}\ ^{2S_f+1}D$ states is exactly -1. Consequently, these photolines would not be observed along the direction of the electric polarization vector. However, under the experimental conditions in modern facilities the angular anisotropy is entirely smeared out.

Author Contributions: Conceptualization M.D.K. and A.N.G.-G.; investigation, formal analysis and visualization M.D.K. and E.V.G.; resources and R-matrix calculations M.D.K., S.M.B. and O.Z.; writing—original draft preparation E.V.G. and M.D.K.; writing—review and editing A.N.G.-G., E.V.G. and M.D.K. All authors have read and agreed to the published version of the manuscript.

Data Availability Statement: Not applicable.

Conflicts of Interest: The authors declare no conflict of interest.

References

1. Cederbaum, L.S.; Tarantelli, F.; Sgamellotti, A.; Schirmer, J. On double vacancies in the core. *J. Chem. Phys.* **1986**, *85*, 6513. [CrossRef]
2. Eland, J.H.D.; Tashiro, M.; Linusson, P.; Ehara, M.; Ueda, K.; Feifel, R. Double Core Hole Creation and Subsequent Auger Decay in NH_3 and CH_4 Molecules. *Phys. Rev. Lett.* **2010**, *105*, 213005. [CrossRef]
3. Berrah, N. Molecular dynamics induced by short and intense x-ray pulses from the LCLS. *Phys. Scr.* **2016**, *T169*, 014001. [CrossRef]
4. Charpak, G.; Hebd, C.R. Molecular single photon double K-shell ionization. *Seances Acad. Sci.* **1953**, *237*, 243.
5. Püttner, R.; Goldsztejn, G.; Céolin, D.; Rueff, J.P.; Moreno, T.; Kushawaha, R.K.; Marchenko, T.; Guillemin, R.; Journel, L.; Lindle, D.W.; et al. Direct Observation of Double-Core-Hole Shake-Up States in Photoemission. *Phys. Rev. Lett.* **2015**, *114*, 093001. [CrossRef] [PubMed]
6. Goldsztejn, G.; Marchenko, T.; Püttner, R.; Journel, L.; Guillemin, R.; Carniato, S.; Selles, P.; Travnikova, O.; Céolin, D.; Lago, A.F.; et al. Double-Core-Hole States in Neon: Lifetime, Post-Collision Interaction, and Spectral Assignment. *Phys. Rev. Lett.* **2016**, *117*, 133001. [CrossRef]
7. Goldsztejn, G.; Püttner, R.; Journel, L.; Guillemin, R.; Travnikova, O.; Cunha de Miranda, B.; Ismail, I.; Carniato, S.; Selles, P.; Céolin, D.; et al. Experimental and theoretical study of the double-core-hole hypersatellite Auger spectrum of Ne. *Phys. Rev. A* **2017**, *96*, 012513. [CrossRef]
8. Perry-Sassmannshausen, A.; Buhr, T.; Borovik, A.; Martins, M.; Reinwardt, S.; Ricz, S.; Stock, S.O.; Trinter, F.; Müller, A.; Fritzsche, S.; et al. Multiple Photodetachment of Carbon Anions via Single and Double Core-Hole Creation. *Phys. Rev. Lett.* **2020**, *124*, 083203. [CrossRef] [PubMed]
9. Schippers, S.; Beerwerth, R.; Abrok, L.; Bari, S.; Buhr, T.; Martins, M.; Ricz, S.; Viefhaus, J.; Fritzsche, S.; Müller, A. Prominent role of multielectron processes in *K*-shell double and triple photodetachment of oxygen anions. *Phys. Rev. A* **2016**, *94*, 041401. [CrossRef]
10. Kuetgens, U.; Hormes, J. Thresholds of the K+L double photoexcitation in argon. *Phys. Rev. A* **1991**, *44*, 264–267. [CrossRef] [PubMed]
11. Štuhec, M.; Kodre, A.; Hribar, M.; Glavič-Cindro, D.; Arčon, I.; Drube, W. Configuration interaction in argon KL resonances. *Phys. Rev. A* **1994**, *49*, 3104–3105. [CrossRef] [PubMed]
12. Dousse, J.C.; Hoszowska, J. *L*- and *M*-shell-electron shake processes following 1*s* photoionization in argon and krypton. *Phys. Rev. A* **1997**, *56*, 4517–4531. [CrossRef]
13. Nakano, M.; Selles, P.; Lablanquie, P.; Hikosaka, Y.; Penent, F.; Shigemasa, E.; Ito, K.; Carniato, S. Near-Edge X-Ray Absorption Fine Structures Revealed in Core Ionization Photoelectron Spectroscopy. *Phys. Rev. Lett.* **2013**, *111*, 123001. [CrossRef] [PubMed]
14. Salén, P.; van der Meulen, P.; Schmidt, H.T.; Thomas, R.D.; Larsson, M.; Feifel, R.; Piancastelli, M.N.; Fang, L.; Murphy, B.; Osipov, T.; et al. Experimental Verification of the Chemical Sensitivity of Two-Site Double Core-Hole States Formed by an X-Ray Free-Electron Laser. *Phys. Rev. Lett.* **2012**, *108*, 153003. [CrossRef]
15. Berrah, N.; Fang, L.; Murphy, B.; Osipov, T.; Ueda, K.; Kukk, E.; Feifel, R.; van der Meulen, P.; Salen, P.; Schmidt, H.T.; et al. Double-core-hole spectroscopy for chemical analysis with an intense X-ray femtosecond laser. *Proc. Natl. Acad. Sci. USA* **2011**, *108*, 16912–16915. [CrossRef]
16. Mazza, T.; Ilchen, M.; Kiselev, M.D.; Gryzlova, E.V.; Baumann, T.M.; Boll, R.; De Fanis, A.; Grychtol, P.; Montaño, J.; Music, V.; et al. Mapping Resonance Structures in Transient Core-Ionized Atoms. *Phys. Rev. X* **2020**, *10*, 041056. [CrossRef]
17. Lambropoulos, P.; Nikolopoulos, G.M.; Papamihail, K.G. Route to direct multiphoton multiple ionization. *Phys. Rev. A* **2011**, *83*, 021407. [CrossRef]
18. Son, S.K.; Young, L.; Santra, R. Impact of hollow-atom formation on coherent x-ray scattering at high intensity. *Phys. Rev. A* **2011**, *83*, 033402. [CrossRef]
19. Hadjipittas, A.; Banks, H.I.B.; Bergues, B.; Emmanouilidou, A. Sequential single-photon and direct two-photon absorption processes for Xe interacting with attosecond XUV pulses. *Phys. Rev. A* **2020**, *102*, 043108. [CrossRef]
20. Yarzhemsky, V.; Sgamellotti, A. Auger rates of second-row atoms calculated by many-body perturbation theory. *J. Electron Spectrosc. Relat. Phenom.* **2002**, *125*, 13–24. [CrossRef]
21. Svensson, S.; Eriksson, B.; Martensson, N.; Wendin, G.; Gelius, U. Electron shake-up and correlation satellites and continuum shake-off distributions in X-Ray photoelectron spectra of the rare gas atoms. *J. Electron Spectrosc. Relat. Phenom.* **1988**, *47*, 327–384. [CrossRef]
22. Chen, M.H. Auger transition rates and fluorescence yields for the double-K-hole state. *Phys. Rev. A* **1991**, *44*, 239–242. [CrossRef] [PubMed]

23. Yoshida, H.; Sasaki, J.; Kawabe, Y.; Senba, Y.; Fanis, A.D.; Oura, M.; Fritzsche, S.; Sazhina, I.P.; Kabachnik, N.M.; Ueda, K. Study of second-step Auger transitions in Auger cascades following 1s → 3p photoexcitation in Ne. *J. Phys. B At. Mol. Opt. Phys.* **2005**, *38*, 465–486. [CrossRef]

24. Gorczyca, T.W. Auger decay of the photoexcited $1 s^{-1}np$ Rydberg series in neon. *Phys. Rev. A* **2000**, *61*, 024702. [CrossRef]

25. Novikovskiy, N.M.; Rezvan, D.V.; Ivanov, N.M.; Petrov, I.D.; Lagutin, B.M.; Knie, A.; Ehresmann, A.; Demekhin, P.V.; Sukhorukov, V.L. Rearrangement of electron shells and interchannel interaction in the K photoabsorption of Ne. *Eur. Phys. J. D* **2019**, *73*, 22. [CrossRef]

26. Southworth, S.H.; Kanter, E.P.; Krässig, B.; Young, L.; Armen, G.B.; Levin, J.C.; Ederer, D.L.; Chen, M.H. Double K-shell photoionization of neon. *Phys. Rev. A* **2003**, *67*, 062712. [CrossRef]

27. Novikov, S.A.; Hopersky, A.N. Two-photon knocking-out of two electrons of the $1s^2$-shell of the neon atom. *J. Phys. B At. Mol. Opt. Phys.* **2002**, *35*, L339–L343. [CrossRef]

28. Kramida, A.; Ralchenko, Y.; Reader, J.; NIST ASD Team (2021). NIST Atomic Spectra Database (version 5.9). 2021. Available online: https://physics.nist.gov/asd (accessed on 30 October 2021).

29. Zatsarinny, O. BSR: B-spline atomic R-matrix codes. *Comput. Phys. Commun.* **2006**, *174*, 273–356. [CrossRef]

30. Fischer, C.F.; Brage, T.; Johnsson, P. *Computational Atomic Structure: An MCHF Approach*; IOP Publishing: Bristol, UK, 1997.

31. Gryzlova, E.V.; Kiselev, M.D.; Popova, M.M.; Zubekhin, A.A.; Sansone, G.; Grum-Grzhimailo, A.N. Multiple Sequential Ionization of Valence n = 4 Shell of Krypton by Intense Femtosecond XUV Pulses. *Atoms* **2020**, *8*, 80. [CrossRef]